Geophysical Research Letters

RESEARCH LETTER
10.1029/2020GL092335

On the Breakdown of ENSO's Relationship With Thermocline Depth in the Central-Equatorial Pacific

Sen Zhao[1,2], Fei-Fei Jin[2], Xiaoyu Long[3], and Mark A. Cane[4]

[1]CIC-FEMD/ILCEC, Key Laboratory of Meteorological Disaster of Ministry of Education, and College of Atmospheric Science, Nanjing University of Information Science and Technology, Nanjing, China, [2]Department of Atmospheric Sciences, University of Hawai'i at Mānoa, Honolulu, HI, USA, [3]Joint Institute for Marine and Atmospheric Research, School of Ocean and Earth Science and Technology, University of Hawai'i at Mānoa, Honolulu, HI, USA, [4]Lamont-Doherty Earth Observatory of Columbia University, Palisades, NY, USA

Abstract Recent classification of El Nino-Southern Oscillation (ENSO) into two types, Eastern (EP) and Central (CP) events, has highlighted the importance of the central Pacific. We show here that the local correlation between ENSO subsurface temperatures (T_{sub}) in the upper 100-m and thermocline depth anomalies breaks down in the central equatorial Pacific, whereas T_{sub} remains well correlated with sea surface height anomalies. This observed difference in the central equatorial Pacific is simulated by almost all climate models. It arises from a vertically slanted T_{sub} anomaly structure that is unique to the central equatorial Pacific. We show that this feature is an adiabatic response to wind-driving that is even present in a linear dynamic model, as long as the model has enough baroclinic modes to adequately represent the observed vertical complexity. Our findings have implications for better understanding the different importance of thermocline feedback in CP and EP events.

Plain Language Summary The El Niño-Southern Oscillation (ENSO) is the most prominent interannual variability of the Earth climate system, strongly affecting the global climate. The variations of subsurface temperature, which is often represented by the fluctuations of thermocline depth and sea surface height interchangeably, play a controlling role in the evolutions of sea surface temperature of ENSO cycle. Here, we show that in the central equatorial Pacific ENSO subsurface temperature correlates poorly with thermocline but well with sea surface height. This observed difference occurs commonly in almost all CMIP6 models. We demonstrate that it arises from a unique vertically slanted distribution of the subsurface temperature in the central Pacific in response to winds associated with ENSO. Our findings may have implications for better understanding diverse behaviors of ENSO events occurring in central and eastern equatorial Pacific.

Key Points:

- In the central equatorial Pacific, El Nino-Southern Oscillation subsurface temperature (T_{sub}) correlates poorly with thermocline depth but well with sea level
- This kind of difference in T_{sub} correlations is a robust feature captured by nearly all climate models
- Wind-driven vertically slanted T_{sub} distribution is largely responsible for this unique feature in the central equatorial Pacific

Supporting Information:

Supporting Information may be found in the online version of this article.

Correspondence to:

F.-F. Jin,
jff@hawaii.edu

Citation:

Zhao, S., Jin, F.-F., Long, X., & Cane, M. A. (2021). On the breakdown of ENSO's relationship with thermocline depth in the central-equatorial Pacific. *Geophysical Research Letters*, *48*, e2020GL092335. https://doi.org/10.1029/2020GL092335

Received 29 DEC 2020
Accepted 28 MAR 2021

1. Introduction

El Nino-Southern Oscillation (ENSO) pattern diversity has been classified into two types or flavors of ENSO, characterized by pronounced (positive or negative) sea surface temperature (SST) anomalies in the eastern equatorial Pacific (EP) or the central equatorial Pacific (CP) (e.g., Ashok et al., 2007; Kao & Yu, 2009; Kug et al., 2009; Ren & Jin, 2013). The SST on the equator is strongly influenced by vertical upwelling and vertical entrainment of subsurface heat through the base of the mixed layer. A key element is the adiabatic vertical advection of subsurface temperature (T_{sub}), a mechanism known in the literature as the "thermocline feedback" (An & Jin, 2001; Cane & Zebiak, 1985; Dewitte et al., 2002; Jin & An, 1999). Strong upwelling and the sharp, shallow thermocline in the EP region make SST variations very sensitive vertical displacement of the thermocline. Thus, the "thermocline feedback" dominates the growth and phase transition of EP El Niño events (An & Jin, 2001; Cane et al., 1990; Jin, 1997a, 1997b; Jin & Neelin, 1993; Jin et al., 2006). In contrast, the CP region has a large climatological zonal SST gradient with a deep mean thermocline. Mean temperature advection by anomalous zonal currents, a process called the "zonal advective feedback," has been suggested to be crucial in the development of a CP El Niño (Kug et al., 2009). However, the relative importance of zonal advective feedback and thermocline feedback for CP El Niño remains a subject of debate (Fedorov et al., 2015; Guan & McPhaden, 2016; Ren & Jin, 2013; Wang & Ren, 2020).

Quantifying the thermocline feedback involves how ENSO SST is influenced by T_{sub} just below the mixed layer (T_d) and how the latter is related to thermocline depth. Assuming the upper ocean thermal structure moves up and down as a unit implies that the evolutions of T_d may be inferred from the fluctuations of thermocline depth or sea surface height (SSH) empirically. In the well-known Zebiak-Cane (ZC) model (Chen et al., 1995, 2004; Zebiak & Cane, 1987), T_d anomalies were assumed directly related to a hyperbolic tangent function of the local thermocline depth anomalies (Zebiak & Cane, 1987). Several more empirical local and nonlocal parameterized relationships have been established between T_d anomalies and thermocline depth anomalies or SSH anomalies (Kang & Kug, 2000; R.-H. Zhang et al., 2003, 2005; Zheng et al., 2006). However, accurately describing T_d using solely knowledge of thermocline depth is problematic and additional considerations including mixing processes appear to be needed (Dewitte et al., 2009; Yuan et al., 2020).

Thermocline depth and SSH are closely related and nearly interchangeable in terms of their associations with ENSO SST (e.g., Rebert et al., 1985; Wyrtki, 1975). (In a 1.5-layer model, such as that in the ZC ENSO model, one is precisely a constant multiple of the other). Though T_{sub} has been related to thermocline depth in the literature thus far, it would seem to be equally valid to relate it to SSH.

In this study, we revisit the relationships of T_{sub} with thermocline depth and SSH anomalies in the tropical Pacific. We find that in the central equatorial Pacific T_{sub} anomalies in the upper 100-m are better related to SSH than to thermocline depth. We further examine the robustness of this observed feature in simulations of climate models and explore its dynamic causes as well as its implication for ENSO dynamics and diversity.

2. Data and Methodology

To take into account that current ocean reanalysis systems contain considerable uncertainties in estimating the subsurface oceanic state, we use monthly ocean temperature and SSH from seven ocean reanalysis products: the German contribution to Estimating the Circulation and Climate of the Ocean version 2 (GECCO2; Köhl, 2015) and version 3 (GECCO3; Köhl, 2020) from Hamburg University; the ocean reanalysis system version 3 (ORAS3; Balmaseda et al., 2008), version 4 (ORAS4; Balmaseda et al., 2013) and version 5 (ORAS5; Zuo et al., 2019) provided by the European Centre for Medium-Range Weather Forecasts; the Predictive Ocean Atmosphere Model for Australia Ensemble Ocean Data Assimilation System (PEODAS; Yin et al., 2011) from the Bureau of Meteorology; and phase 2.2.4 of the Simple Ocean Data Assimilation (SODA 2.2.4; Carton & Giese, 2008). All products are linearly interpolated to a $1° \times 1°$ horizontal resolutions. As in much earlier work, we take the depth of the 20°C isotherm (D20) as the thermocline depth in the tropical Pacific (Kessler, 1990). The analysis period is from 1961 to 2018. All anomalies are relative to the climatology of the whole period and linearly detrended in order to focus on interannual variability. (Though results are little changed if we do not detrend.) We will refer to the ensemble mean of the reanalysis products as "observations." We also examine the historical simulations of 44 CMIP6 models (Table S1).

We used an ocean general circulation model (OGCM), the ocean component of the Community Earth System Model, the Parallel Ocean Program version 2 (POP2; Smith et al., 2010). We conducted two experiments. In the control simulation (POP2_CTL), the OGCM is forced directly by daily mean surface fluxes of momentum, latent and sensible heat, shortwave and longwave radiative, and freshwater from the JRA55-do product (Tsujino et al., 2018). The model was spin-up for 60 years. We prescribe all these observed fluxes for the period of 1958–2017. In the perturbation simulation (POP2_MF), we prescribe only momentum flux from the interannual data and set other fluxes to climatology.

We also used a dynamical ocean model, which is basically McCreary's (1981, 1996, 2007) linear continuously stratified ocean model, extended to the all tropical oceans with a more realistic coastline and a space dependent background stratification (see Text S1 in supporting information for details). The shallow water equations are solved separately for each baroclinic mode, and the total solution is the linear sum of low-order baroclinic modes. It has been shown that the stratified model with two (or more) baroclinic modes performs significantly better than the 1.5-layer reduced gravity model (Busalacchi & Cane, 1985; Cane, 1984; Dewitte, 2000; Seager et al., 2019). Using both local vertical modes and spatially varying wind projection coefficients based on the WKBJ approximation gives a noticeably more realistic sea level and current structure (Keenlyside & Kleeman, 2002).

3. Observed and Simulated Relationships of T_{sub} With SSH and D20

We first focus on T_{sub} at 75-m (T_{75}), which represents T_{sub} beneath the mixed later and so plays a key role in mixed layer SST budget analyses. As shown Figures 1A and 1B, D20-T_{75} scatterplots show very high correlations in the Niño-3 region ($r = 0.97$) but a weak correlation in Niño-4 region ($r = 0.27$). Similar differences are also found in D20-SST correlations in these two regions (Harrison & Vecchi, 2001). In contrast, the SSH-T_{75} relationships in both regions are strong and linear ($r = 0.98$ and 0.81 for Niño-3 and 4 regions, respectively, Figures 1C and 1D). The marked difference in the correlations between the D20 and SSH with T_{75} in Niño-4 region has been largely overlooked.

Figures 1E–1G and 1H–1J compare the D20-T_{sub} and SSH-T_{sub} relationships in horizontal, vertical, and lead-lag distribution maps. As expected, D20 and T_{sub} are well correlated near and above the mean depth of the 20°C isotherm and broadly in the equatorial Pacific. However, there is a clear minimum in the correlation values, $r < 0.4$, in the Niño-4 region above 100-m (Figures 1E and 1F). Additionally, D20 and T_{75} are nearly in phase in both the eastern Pacific and western Pacific, but a significant delay of T_{75} appears in the central Pacific, with a much lower maximum correlation at positive lag ($r < 0.4$, Figure 1G). For the SSH-T_{sub} correlation the local "hole" in the Niño-4 region is much reduced, especially below 50-m ($r > 0.8$) (Figures 1H–1J). Elsewhere, correlations in the upper 100-m are largely comparable with those for D20-T_{sub} and are slightly better in far west Pacific (Figure 1I). Moreover, SSH and T_{75} are nearly in phase with maximum correlations well above 0.8 over all longitudes (Figure 1J), again highlighting its difference from D20-T_{75} lead-lag relationships in the central Pacific. This difference holds if we take thermocline depth to be the depth of the maximum vertical temperature gradient instead of D20 (Figure S1, Yang & Wang, 2009).

The significant differences in the central Pacific D20-T_{75} and SSH-T_{75} relationships can be clearly seen in EP and CP ENSO composites for both warm and cold events (Ashok et al., 2007; Kao & Yu, 2009; Kug et al., 2009; Ren & Jin, 2011; W. Zhang et al., 2019). As shown in Figure S2, anomalous D20 in this region is nearly zero for CP events and very weakly correlated but out of phase with both T_{75} and SST for EP events, which is consistent with the "hole" in the correlation maps seen in Figures 1E and 1F. In contrast, anomalous SST and T_{75} have a good in-phase correspondence with SSH for CP events. For EP events, T_{75} also maintains a local correspondence to SSH in spite of a spatial sign change within the Niño-4 box region. Thus, SSH has a robust relation with T_{75} in the Niño-4 region regardless of ENSO type, while D20 fails to represent T_{75}.

To isolate this difference between D20-T_{75} and SSH-T_{75} relationships, we calculate the correlation difference (~partial correlation) defined as $r' = r(T_{75},\text{SSH}) - r(T_{75},\text{D20})*r(\text{D20},\text{SSH})$, where $r(x, y)$ denotes the local correlation coefficient between x and y. As shown in Figure 2A, large values of r' are largely confined in Niño-4 region in the central equatorial Pacific. This difference in the Niño-4 region is simulated by climate models, as shown the multi-model ensemble mean of 44 CMIP6 models (Figures 2B and S3).

4. Wind-Driven Vertically Slanted T_{sub} Responses in the Central Equatorial Pacific

Our hypothesis is that ENSO's D20, SSH and T_{sub} anomalies are dynamically driven by wind stress forcing. Thus the adiabatic response to the wind stress is the hypothesized cause of the significant differences in observed and simulated D20-T_{75} and SSH-T_{75} relationships in the central equatorial Pacific. (These differences are found in observations, most CMIP6 models, and all the new simulations reported here.) We carried out twin OGCM experiments, shown in Figure 3. The POP2_CTL simulation, which is forced with observed full surface fluxes captures the observed El Niño evolution. The POP2_MF simulation, in which only the momentum fluxes vary interannually, captures the evolution almost as well, including SSH, thermocline depth and T_{sub} variations in the equatorial band. The exception is the simulation of SST and the near surface layer (Figure 3, especially panel F). That both experiments clearly capture the observed correlation difference between the D20-T_{75} and SSH-T_{75} relationships (Figures 2C and 2D), indicates that this difference is dynamically wind-driven. (Observed relationships of T_{sub} with both SSH and D20 are all simulated in both model runs; see Figures S4 and S5.)

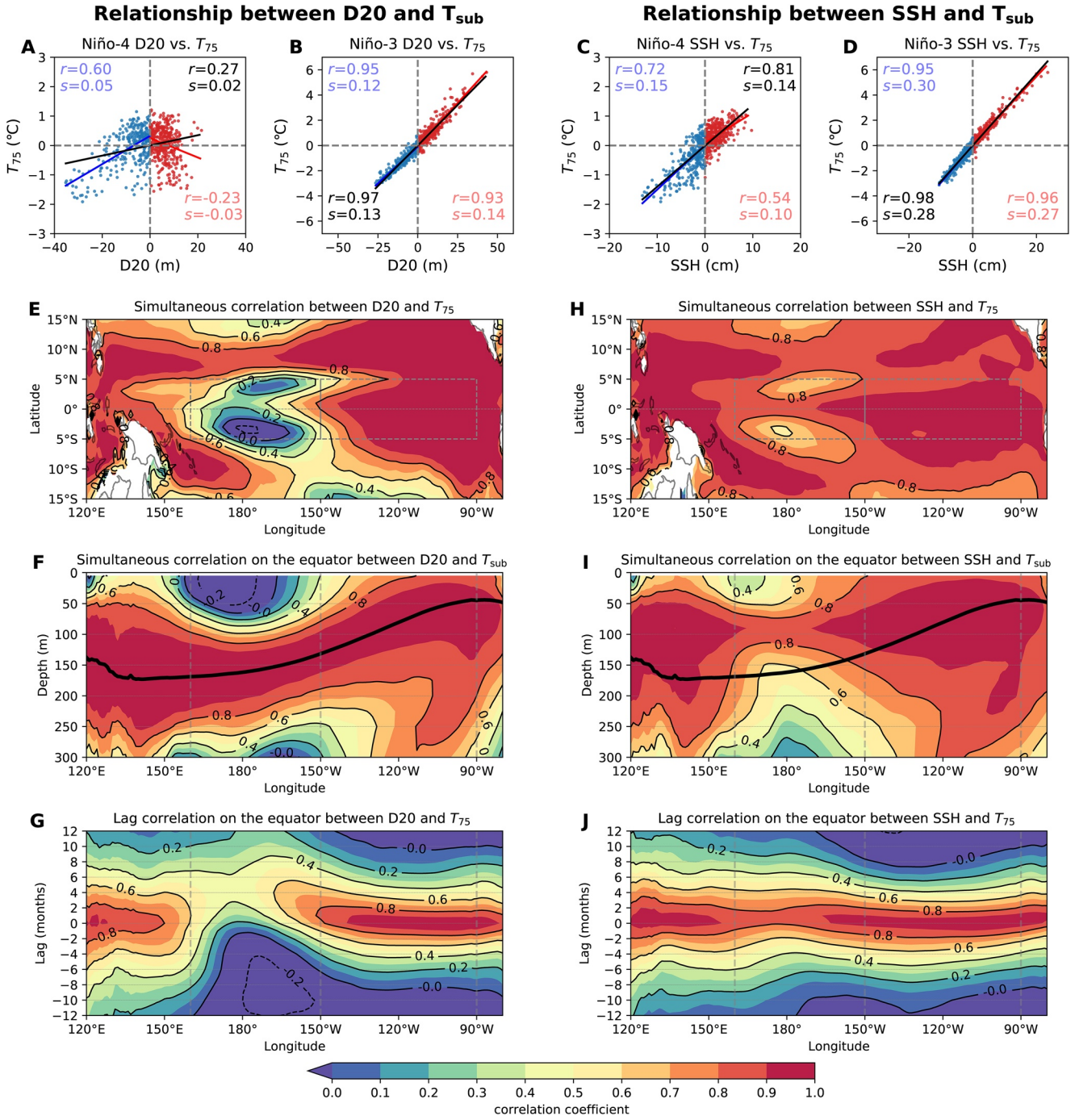

Figure 1. Observed local relationships of T_{sub} anomalies with D20 anomalies and SSH anomalies. Scatterplots of monthly T_{75} anomalies plotted against (A, B) D20 anomalies and (C, D) SSH anomalies over (A, C) Niño-4 region and (B, D) Niño-3 region, respectively. The red, blue, and black lines denote the linear regression for the positive, negative, and all values of abscissa, respectively, and their correlation (r) and slope (s) are indicated in the corresponding color. (E) Simultaneous correlations of T_{75} anomalies with local D20 anomalies. (F) Simultaneous correlations of equatorial T_{sub} anomalies with local D20 anomalies. (G) Lag correlations between equatorial T_{75} anomalies with local D20 anomalies. (H–J) Same as (E–G), respectively, but for SSH anomalies. Equatorial mean is averaged over 2°S-2°N. A positive lag means D20 (SSH) is leading T_{75}. Bold black lines in (F, I) indicate the depth of climatological mean thermocline.

The simulated magnitude of SST anomalies in POP2_MF is stronger than in POP2_CTL (Figures 3B, 3C, and 3F). Differences in T_{sub}, which are limited to the near surface, are attributable to the absence of anomalous heat fluxes in the POP2_MF simulation. The heat fluxes damp the growth of ENSO SST anomalies

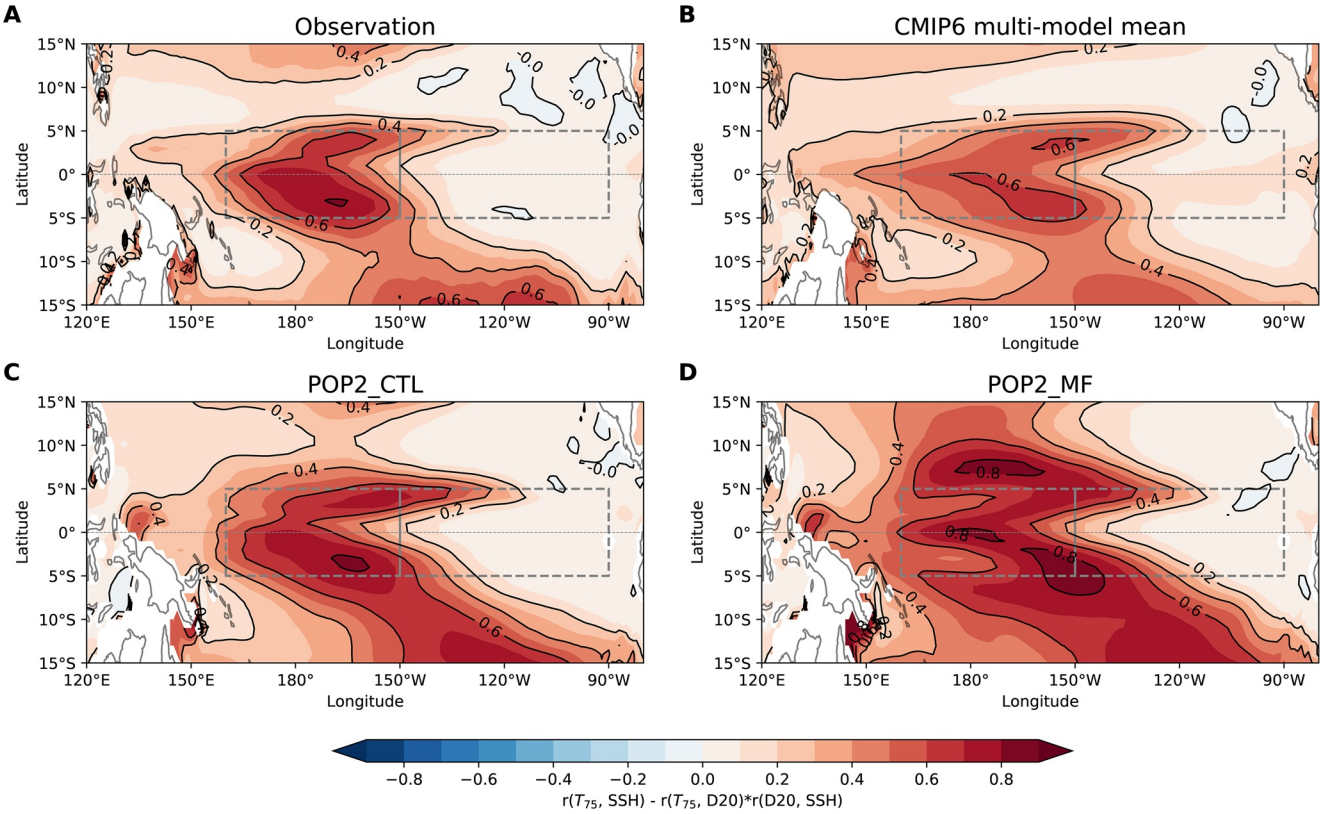

Figure 2. Correlation difference between D20-T_{75} and SSH-T_{75} relationships defined as $r(T_{75},\text{SSH})-r(T_{75},\text{D20})*r(\text{D20},\text{SSH})$, where $r(x, y)$ denotes the local correlation coefficient between x and y. (A) Observation, (B) multi-model ensemble means of 44 CMIP6 models, (C) the POP2_CTL, and (D) POP2_MF simulations. Dashed boxes indicate the Niño-3 and Niño-4 regions.

and their effect is spread downward by mixing processes to about 100-m depth (Figure S6). Because this thermodynamic effect is suppressed in POP2_MF, the correlation difference between D20-T_{75} and SSH-T_{75} in the central equatorial Pacific is slightly strengthened (Figure 2D), but this is a minor effect.

One striking feature in Figures 3A–3C is the vertically slanted T_{sub} anomaly structure unique to the central Pacific, with positive anomalies on top and negative anomalies wedged in below during the El Niño peak phase. This vertically slanted T_{sub} structure in the central Pacific occurs regardless of types and warm or cold phases of ENSO events (Figure S7). Both POP2_CTL and POP2_MF simulations capture this structure well, suggesting this feature is wind-driven. The region of this vertically slanted T_{sub} structure is largely between the magenta and orange vertical lines which correspond to the D20 nodal point and the nodal point of T_{sub} at 50-m (T_{50}) respectively, as highlighted in Figures 3A–3C. These two nodal points changes modestly following warm/cold phases and types of ENSO (Figure S7) but remain largely confined to the Niño-4 region. Outside this region both SSH and D20 are positively correlated with both SST and T_{75}, while within this region, D20's relationships with both SST and T_{75} become blurred and dependent on ENSO phases and types with weak correlations overall.

In contrast, SSH has its node point much closer to T_{50} and thus SSH maintains strong positive correlations with both SST and T_{75} throughout the entire equatorial Pacific, with only a minor reduction in the Niño-4 region. As first shown by Wyrtki (1975), at seasonal and interannual time scales, SSH is dominated by the steric variations of density in the water column. Thus, we may derive SSH anomalies from T_{sub} anomalies above 300-m according to $\eta'_{\text{thermal}} = \int_{-300}^{0} \alpha T' dz$, where $\alpha = -\frac{1}{\rho}\left(\frac{\partial \rho}{\partial T}\right)_{S,p}$ is a thermal expansion coefficient. Here, we computed α based on the climatological mean state (Figure S8A). This η'_{thermal} is highly correlated

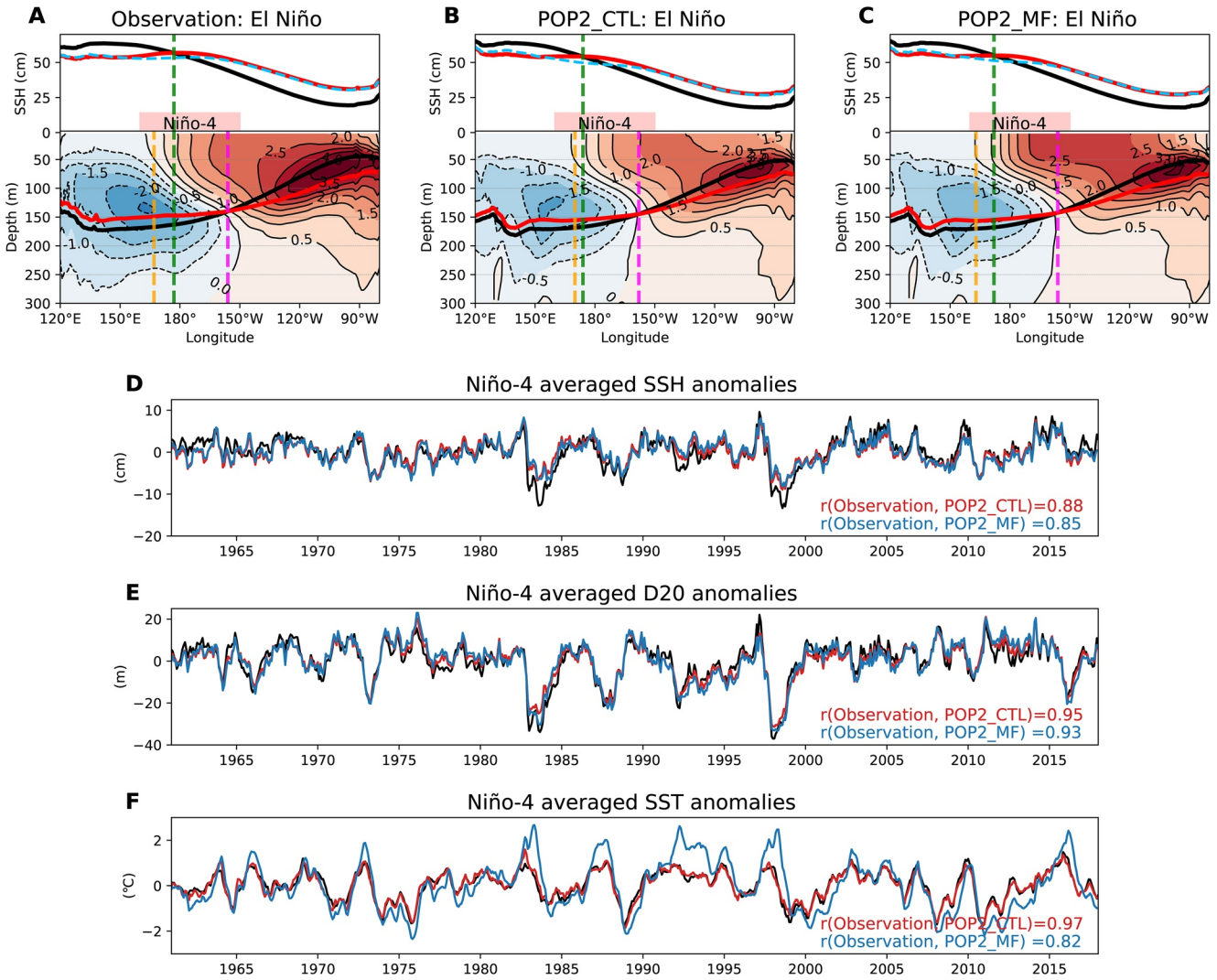

Figure 3. (A–C) Composites of T_{sub} anomalies (*contour shading*), SSH and D20 (*red curves*) on the equator (2°S-2°N) during the peak phase (November–December–January) of El Niño events for (A) observation, (B) POP2_CTL simulations forced with all atmospheric fluxes, and (C) POP2_MF simulations forced with only momentum fluxes. The selected 10 strongest events are 1997/1998, 1982/1983, 2015/2016, 1972/1973, 1991/1992, 2009/2010, 2002/2003, 1965/1966, 1994/1995, 1986/1987 based on the Niño-3.4 index. *Black bold* curves denote climatological mean SSH and D20 for reference; Orange, green, and magenta dashed vertical reference lines indicate the longitudes of zero value of the composite T_{sub} at 50-m, SSH and D20 anomalies, respectively. The blue dashed curves denote the SSH derived from the thermal expansion expression of $\int_{-300}^{0} \overline{\alpha} T' dz$ adding on the climatological mean SSH. Pink shading boxes indicate Niño-4 longitudes. Time series of Niño-4 averaged (D) SSH anomalies, (E) D20 anomalies, and (F) SST anomalies for observation (*black*), POP2_CTL (*red*), and POP2_MF (*blue*) simulations. Correlation coefficients are shown at the bottom right of panels.

with the observed total SSH anomalies within the tropics (Figure S8B), as expected from Wyrtki (1975). In particular, the Niño-4 averaged η'_{thermal} closely follows the observed SSH anomalies ($r = 0.94$, slope $= 0.98$, Figure S8C). Since the thermal expansion coefficient increases with temperature, the climatological mean thermal expansion coefficient $\overline{\alpha}$ increases toward the surface. Therefore, SSH anomalies, an integral of T_{sub} anomalies, gives more weight to near surface temperatures, and so is more representative of the variations of T_{sub} anomalies in the upper 100-m. The vertically slanted T_{sub} structure that is unique to the Niño-4 region greatly weakens the coupling between D20 and the temperature structure nearer to the surface. This slanted structure is absent in other regions of the equatorial oceans, so this coupling remains strong elsewhere, and the D20-T_{sub} and SSH-T_{sub} relationships are roughly equally strong. It is the unique slanted nature of T_{sub} anomalies in the central Pacific that is responsible for the difference between D20-T_{sub} and SSH-T_{sub} relationship observed in nature and simulated in climate models.

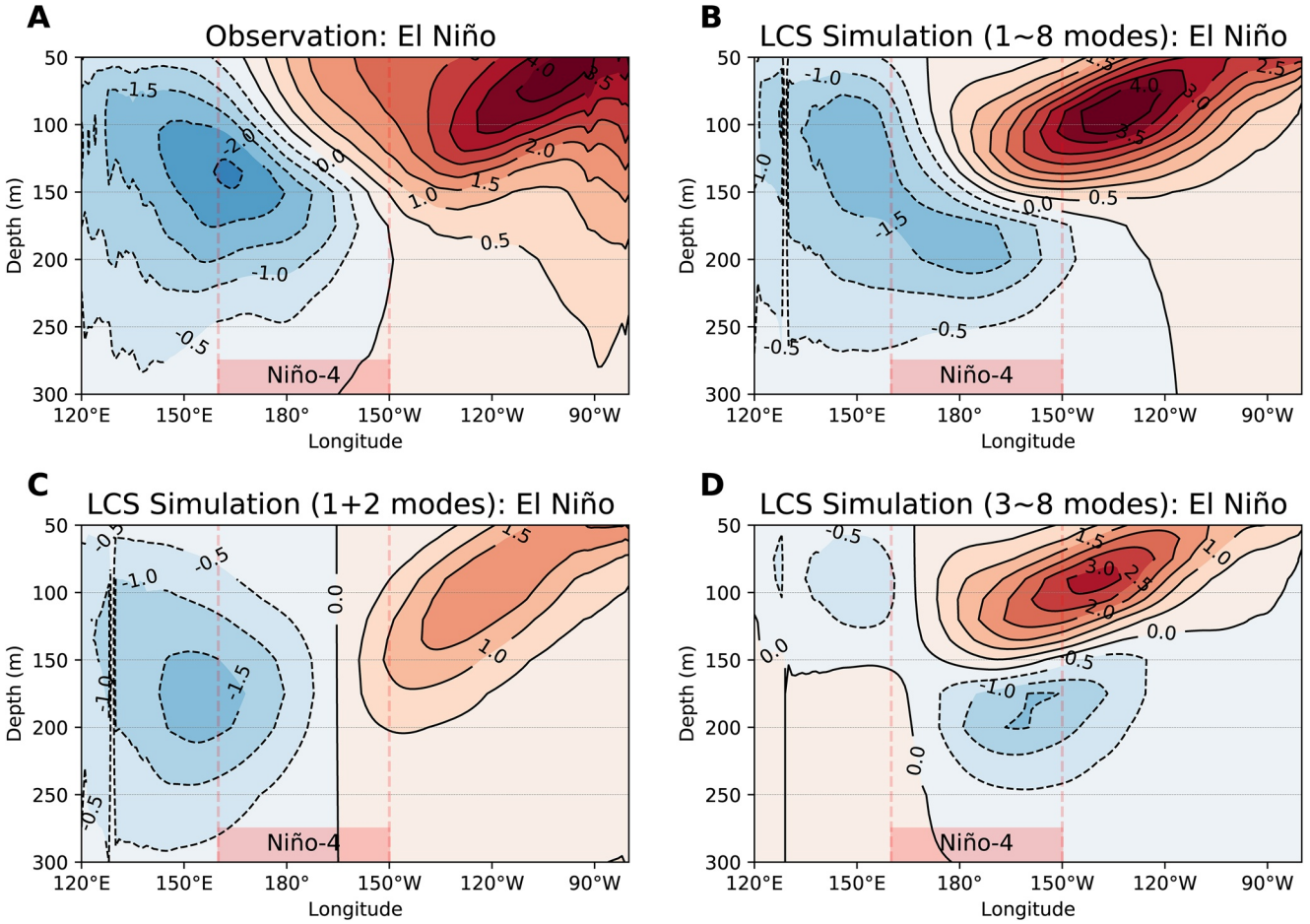

Figure 4. Contribution of high-order vertical modes is responsible for vertically slanted T_{sub} responses in the central equatorial Pacific. Composites of T_{sub} anomalies on the equator (2°S-2°N) during the peak phase (November–December–January) of (A) El Niño events for observation, (B) LCS simulation with 1~8 vertical modes, (C) 1 + 2 vertical modes, and (D) 3~8 vertical modes. Pink shading boxes indicate Niño-4 longitudes.

Next, we address the dynamical cause of the vertically slanted T_{sub} responses in the central equatorial Pacific. As before, our hypothesis is that it is a consequence of wind-driven adiabatic ocean dynamics, with the added condition that the dynamics are linear. To explore this, we use a linear continuously stratified ocean model (LCS) with spatially varying background (climatological) stratification (see supporting information text for details). It is driven solely by observed JRA55-do wind stress. Given the observational evidence that density anomalies are largely dominated by the thermal expansion effect (Figure S8; Wyrtki 1975), T_{sub} anomalies below the mixed layer can be approximated as a function of the contribution of the baroclinic modes to SSH anomalies (see Equation 8 in supporting information text; Dewitte et al., 2009). Figure 4 shows that during the peak phase of El Niño events, the observed vertically slanted T_{sub} structure in the central equatorial Pacific is clearly reproduced in the LCS with eight vertical modes (Figure 4B) but is absent in the LCS with 2 modes (Figure 4C). Figure 4D shows that the contribution of modes 3–8 increases the stratification in the central Pacific during the El Niño peak phase, indicating that high-order vertical modes are responsible for the vertically slanted temperature response in the central equatorial Pacific.

5. Conclusion and Discussions

The fluctuations of thermocline depth (D20) and sea surface height (SSH), often used interchangeably to represent slow variations of the upper ocean thermal state, play a central role in our understanding of ENSO cycles. In this study, however, we find that the close linkage between thermocline depth and

temperatures above 100-m breaks down in the central equatorial Pacific, while these temperatures remain well correlated with SSH. In the Niño-4 region the D20-T_{75} relationship varies with ENSO phases and types, and consequently a "hole" of weak D20-T_{75} correlation occurs. The difference between D20-T_{75} and SSH-T_{75} correlations in the central Pacific is also common to most climate model simulations. This difference is well simulated in two OGCM experiments, one driven by monthly variations in all surface fluxes, the other where only the wind stress varies from year to year. Both create a unique vertically slanted T_{sub} structure in the central equatorial Pacific, demonstrating that this structure is dynamically driven by ENSO wind stress forcing. The slanted structure is responsible for the difference between D20-T_{sub} and SSH-T_{sub} correlations observed in nature and simulated in climate models. We further demonstrate that high-order vertical modes are critical for this unique vertically slanted T_{sub} responses in the central equatorial Pacific.

The central Pacific "hole" is still present in the SSH-T_{sub} correlation (Figures 1H and 1I), though less deep than for D20-T_{sub}. The weak and blurred D20-T_{sub} and SSH-T_{sub} relationships in the central Pacific stem from a vertically slanted T_{sub} regional structure that is not seen elsewhere in the equatorial Pacific. It makes the thermocline feedback less effective in the central Pacific than in the eastern Pacific, which leaves room for other influences on central Pacific SST, in particular the zonal advective feedback mechanism. Equatorial zonal geostrophic currents follow the second order y-derivative of equatorial SSH well, but the latter is again well correlated with the second order y-derivative of equatorial thermocline depth outside of the central Pacific (Figure S9; Su et al., 2010). The unique difference of D20-T_{sub} and SSH-T_{sub} there may contribute to ENSO pattern diversity (e.g., Kug et al., 2009; Ren & Jin, 2013). Great spreads among climate model simulations of the locations and intensities of the hole in D20-T_{75} (not shown) may be contributing to the differences in ENSO patterns among the models.

Our findings prompt some reconsideration of the phrase "thermocline feedback." Taken in its greatest generality, it is a shorthand for the connection between the dynamical changes in upper ocean thermal structure driven by wind stress and the near-surface thermodynamics that determine SST. In the pioneering ENSO model of Zebiak and Cane (1987) this connection was made by parameterizing the temperature just below the mixed layer, T_d, as a function of thermocline depth, D20. In their reduced gravity 1.5-layer dynamics, thermocline depth and SSH are perfectly interchangeable. Our results here show that taking $T_d = T_d$(D20) works quite well almost everywhere along the equator. The exception is the central Pacific, where it would have been better to take $T_d = T_d$(SSH), though to be an improvement requires that the model have multiple vertical modes, not just a single one as in the ZC model. What is done in ZC amounts to assuming that wind-driven dynamics moves the temperature structure of the upper ocean vertically as a single unit, with no internal stretching or compressing of isotherms. This approximation succeeds almost everywhere, falling short in the central Pacific, the key region for CP ENSO events.

The implications of our findings for our understanding of the role of ocean dynamics in ENSO's SST evolution in the central Pacific, and thus for the dynamics of ENSO diversity, have yet to be fully worked out. The unique vertically slanted T_{sub} structure in the central Pacific has not been included in the simple to intermediate coupled models that have led to much progress in ENSO theory. Consideration of this observed unique ENSO structure is a promising pathway for further understanding of ENSO diversity and complexity (Timmermann et al., 2018), as well as for improving ENSO simulations in climate models.

Data Availability Statement

All data sets used in this study are publicly available: the GECCO2 at https://icdc.cen.uni-hamburg.de/en/gecco2.html; the GECCO3 at https://icdc.cen.uni-hamburg.de/en/gecco3.html; the ORAS3 at http://apdrc.soest.hawaii.edu/dods/public_data/Reanalysis_Data/ORA-S3; the ORAS4 at http://apdrc.soest.hawaii.edu/dods/public_data/Reanalysis_Data/ORAS4; the ORAS5 at http://apdrc.soest.hawaii.edu/dods/public_data/Reanalysis_Data/ORAS5; the PEODAS at http://opendap.bom.gov.au:8080/thredds/catalogs/bmrc-poama-catalog.html; the SODA 2.2.4 at http://apdrc.soest.hawaii.edu/dods/public_data/SODAhttp://apdrc.soest.hawaii.edu/dods/public_data/SODA; CMIP6 historical simulations at https://esgf-node.llnl.gov/projects/cmip6/; the JRA55-do fluxes at https://esgf-node.llnl.gov/search/input4mips/.

Acknowledgments
We thank two anonymous reviewers for their valuable comments and suggestions, and L. Geng for the helpful discussion. This research was supported by the U.S. National Science Foundation (AGS-1813611 and AGS-1406601) and U.S. Department of Energy (DE-SC0005110). M. A. Cane was supported by NSF award OCE-1657209. The authors acknowledge the FAIR data policy.

References

An, S.-I., & Jin, F.-F. (2001). Collective role of thermocline and zonal advective feedbacks in the ENSO mode. *Journal of Climate*, *14*(16), 3421–3432. https://doi.org/10.1175/1520-0442(2001)014<3421:crotaz>2.0.co;2

Ashok, K., Behera, S. K., Rao, S. A., Weng, H. Y., & Yamagata, T. (2007). El Niño Modoki and its possible teleconnection. *Journal of Geophysical Research*, *112*, C11007. https://doi.org/10.1029/2006jc003798

Balmaseda, M. A., Mogensen, K., & Weaver, A. T. (2013). Evaluation of the ECMWF ocean reanalysis system ORAS4. *Quarterly Journal of the Royal Meteorological Society*, *139*(674), 1132–1161. https://doi.org/10.1002/qj.2063

Balmaseda, M. A., Vidard, A., & Anderson, D. L. T. (2008). The ECMWF ocean analysis system: ORA-S3. *Monthly Weather Review*, *136*(8), 3018–3034. https://doi.org/10.1175/2008mwr2433.1

Busalacchi, A. J., & Cane, M. A. (1985). Hindcasts of sea level variations during the 1982-83 El Niño. *Journal of Physical Oceanography*, *15*(2), 213–221. https://doi.org/10.1175/1520-0485(1985)015<0213:hoslvd>2.0.co;2

Cane, M. A. (1984). Modeling sea level during El Niño. *Journal of Physical Oceanography*, *14*(12), 1864–1874. https://doi.org/10.1175/1520-0485(1984)014<1864:mslden>2.0.co;2

Cane, M. A., Münnich, M., & Zebiak, S. F. (1990). A study of self-excited oscillations of the tropical ocean-atmosphere system. Part I: Linear analysis. *Journal of the Atmospheric Sciences*, *47*(13), 1562–1577. https://doi.org/10.1175/1520-0469(1990)047<1562:asoseo>2.0.co;2

Cane, M. A., & Zebiak, S. E. (1985). A theory for El Nino and the Southern Oscillation. *Science*, *228*(4703), 1085–1087. https://doi.org/10.1126/science.228.4703.1085

Carton, J. A., & Giese, B. S. (2008). A reanalysis of ocean climate using simple ocean data assimilation (SODA). *Monthly Weather Review*, *136*(8), 2999–3017. https://doi.org/10.1175/2007mwr1978.1

Chen, D., Cane, M. A., Kaplan, A., Zebiak, S. E., & Huang, D. (2004). Predictability of El Niño over the past 148 years. *Nature*, *428*(6984), 733–736. https://doi.org/10.1038/nature02439

Chen, D., Zebiak, S. E., Busalacchi, A. J., & Cane, M. A. (1995). An improved procedure for El Nino forecasting: Implications for predictability. *Science*, *269*(5231), 1699–1702. https://doi.org/10.1126/science.269.5231.1699

Dewitte, B. (2000). Sensitivity of an intermediate ocean-atmosphere coupled model of the tropical Pacific to its oceanic vertical structure. *Journal of Climate*, *13*(13), 2363–2388. https://doi.org/10.1175/1520-0442(2000)013<2363:soaioa>2.0.co;2

Dewitte, B., Gushchina, D., duPenhoat, Y., & Lakeev, S. (2002). On the importance of subsurface variability for ENSO simulation and prediction with intermediate coupled models of the Tropical Pacific: A case study for the 1997–1998 El Niño. *Geophysical Research Letters*, *29*(14), 1666. https://doi.org/10.1029/2001gl014452

Dewitte, B., Thual, S., Yeh, S.-W., An, S.-I., Moon, B.-K., & Giese, B. S. (2009). Low-frequency variability of temperature in the vicinity of the equatorial Pacific thermocline in SODA: Role of equatorial wave dynamics and ENSO asymmetry. *Journal of Climate*, *22*(21), 5783–5795. https://doi.org/10.1175/2009jcli2764.1

Fedorov, A. V., Hu, S., Lengaigne, M., & Guilyardi, E. (2015). The impact of westerly wind bursts and ocean initial state on the development, and diversity of El Niño events. *Climate Dynamics*, *44*(5–6), 1381–1401. https://doi.org/10.1007/s00382-014-2126-4

Guan, C., & McPhaden, M. J. (2016). Ocean processes affecting the twenty-first-century shift in ENSO SST variability. *Journal of Climate*, *29*(19), 6861–6879. https://doi.org/10.1175/jcli-d-15-0870.1

Harrison, D. E., & Vecchi, G. A. (2001). El Niño and La Niña-equatorial Pacific thermocline depth and sea surface temperature anomalies, 1986-98. *Geophysical Research Letters*, *28*(6), 1051–1054. https://doi.org/10.1029/1999gl011307

Jin, F.-F. (1997a). An equatorial ocean recharge paradigm for ENSO. Part I: Conceptual model. *Journal of the Atmospheric Sciences*, *54*, 811–829. https://doi.org/10.1175/1520-0469(1997)054<0811:aeorpf>2.0.co;2

Jin, F.-F. (1997b). An equatorial ocean recharge paradigm for ENSO. Part II: A stripped-down coupled model. *Journal of the Atmospheric Sciences*, *54*, 830–847. https://doi.org/10.1175/1520-0469(1997)054<0830:aeorpf>2.0.co;2

Jin, F.-F., & An, S.-I. (1999). Thermocline and zonal advective feedbacks within the equatorial ocean recharge oscillator model for ENSO. *Geophysical Research Letters*, *26*(19), 2989–2992. https://doi.org/10.1029/1999gl002297

Jin, F.-F., Kim, S. T., & Bejarano, L. (2006). A coupled-stability index for ENSO. *Geophysical Research Letters*, *33*, L23708. https://doi.org/10.1029/2006gl027221

Jin, F.-F., & Neelin, J. D. (1993). Modes of interannual tropical ocean-atmosphere interaction - A unified view. Part I: Numerical results. *Journal of the Atmospheric Sciences*, *50*(21), 3477–3503. https://doi.org/10.1175/1520-0469(1993)050<3477:moitoi>2.0.co;2

Kang, I.-S., & Kug, J.-S. (2000). An El-Nino prediction system using an intermediate ocean and a statistical atmosphere. *Geophysical Research Letters*, *27*(8), 1167–1170. https://doi.org/10.1029/1999gl011023

Kao, H.-Y., & Yu, J.-Y. (2009). Contrasting Eastern-Pacific and Central-Pacific types of ENSO. *Journal of Climate*, *22*, 615–632. https://doi.org/10.1175/2008jcli2309.1

Keenlyside, N., & Kleeman, R. (2002). Annual cycle of equatorial zonal currents in the Pacific. *Journal of Geophysical Research*, *107*(C8), 8-1–8-13. https://doi.org/10.1029/2000jc000711

Kessler, W. S. (1990). Observations of long Rossby waves in the northern tropical Pacific. *Journal of Geophysical Research*, *95*(C4), 5183–5217. https://doi.org/10.1029/jc095ic04p05183

Köhl, A. (2015). Evaluation of the GECCO2 ocean synthesis: Transports of volume, heat and freshwater in the Atlantic. *Quarterly Journal of the Royal Meteorological Society*, *141*(686), 166–181. https://doi.org/10.1002/qj.2347

Köhl, A. (2020). Evaluating the GECCO3 1948-2018 ocean synthesis – A configuration for initializing the MPI-ESM climate model. *Quarterly Journal of the Royal Meteorological Society*, *146*(730), 2250–2273. https://doi.org/10.1002/qj.3790

Kug, J.-S., Jin, F.-F., & An, S.-I. (2009). Two types of El Niño events: Cold tongue El Niño and warm pool El Niño. *Journal of Climate*, *22*(6), 1499–1515. https://doi.org/10.1175/2008jcli2624.1

McCreary, J. P. (1981). A linear stratified ocean model of the equatorial undercurrent. *Philosophical Transactions of the Royal Society of London - Series A: Mathematical and Physical Sciences*, *298*(1444), 603–635. https://doi.org/10.1098/rsta.1981.0002

McCreary, J. P., Han, W., Shankar, D., & Shetye, S. R. (1996). Dynamics of the East India coastal current: 2. Numerical solutions. *Journal of Geophysical Research*, *101*(C6), 13993–14010. https://doi.org/10.1029/96jc00560

McCreary, J. P., Miyama, T., Furue, R., Jensen, T., Kang, H.-W., Bang, B., & Qu, T. (2007). Interactions between the Indonesian throughflow and circulations in the Indian and Pacific Oceans. *Progress in Oceanography*, *75*(1), 70–114. https://doi.org/10.1016/j.pocean.2007.05.004

Rebert, J. P., Donguy, J. R., Eldin, G., & Wyrtki, K. (1985). Relations between sea level, thermocline depth, heat content, and dynamic height in the tropical Pacific Ocean. *Journal of Geophysical Research*, *90*(C6), 11719–11725. https://doi.org/10.1029/jc090ic06p11719

Ren, H.-L., & Jin, F.-F. (2011). Niño indices for two types of ENSO. *Geophysical Research Letters*, *38*(4), L04704. https://doi.org/10.1029/2010gl046031

Ren, H.-L., & Jin, F.-F. (2013). Recharge oscillator mechanisms in two types of ENSO. *Journal of Climate*, *26*(17), 6506–6523. https://doi.org/10.1175/jcli-d-12-00601.1

Seager, R., Cane, M., Henderson, N., Lee, D.-E., Abernathey, R., & Zhang, H. (2019). Strengthening tropical Pacific zonal sea surface temperature gradient consistent with rising greenhouse gases. *Nature Climate Change*, *9*(7), 517–522. https://doi.org/10.1038/s41558-019-0505-x

Smith, R., Jones, P., Briegleb, B., Bryan, F., Danabasoglu, G., Dennis, J., et al. (2010). *The Parallel Ocean Program (POP) reference manual: Ocean component of the Community Climate System Model (CCSM) and Community Earth System Model (CESM)* (Tech. Rep. No. LAUR-10-01853) (p. 140). Los Alamos: Los Alamos National Laboratory. Retrieved from http://www.cesm.ucar.edu/models/cesm1.2/pop2/doc/sci/POPRefManual.pdf

Su, J., Zhang, R., Li, T., Rong, X., Kug, J.-S., & Hong, C.-C. (2010). Causes of the El Niño and La Niña amplitude asymmetry in the equatorial eastern Pacific. *Journal of Climate*, *23*(3), 605–617. https://doi.org/10.1175/2009jcli2894.1

Timmermann, A., An, S.-I., Kug, J.-S., Jin, F.-F., Cai, W., Capotondi, A., et al. (2018). El Niño–Southern Oscillation complexity. *Nature*, *559*(7715), 535–545. https://doi.org/10.1038/s41586-018-0252-6

Tsujino, H., Urakawa, S., Nakano, H., Small, R. J., Kim, W. M., Yeager, S. G., et al. (2018). JRA-55 based surface dataset for driving ocean-sea-ice models (JRA55-do). *Ocean Modelling*, *130*, 79–139. https://doi.org/10.1016/j.ocemod.2018.07.002

Wang, R., & Ren, H.-L. (2020). Understanding key roles of two ENSO modes in spatiotemporal diversity of ENSO. *Journal of Climate*, *33*(15), 6453–6469. https://doi.org/10.1175/jcli-d-19-0770.1

Wyrtki, K. (1975). Fluctuations of the dynamic topography in the Pacific Ocean. *Journal of Physical Oceanography*, *5*(3), 450–459. https://doi.org/10.1175/1520-0485(1975)005<0450:fotdti>2.0.co;2

Yang, H., & Wang, F. (2009). Revisiting the thermocline depth in the equatorial Pacific. *Journal of Climate*, *22*(13), 3856–3863. https://doi.org/10.1175/2009jcli2836.1

Yin, Y., Alves, O., & Oke, P. R. (2011). An ensemble ocean data assimilation system for seasonal prediction. *Monthly Weather Review*, *139*(3), 786–808. https://doi.org/10.1175/2010mwr3419.1

Yuan, X., Jin, F.-F., & Zhang, W. (2020). A concise and effective expression relating subsurface temperature to the thermocline in the equatorial Pacific. *Geophysical Research Letters*, *47*(15), e2020GL087848. https://doi.org/10.1029/2020gl087848

Zebiak, S. E., & Cane, M. A. (1987). A model El Niñ-Southern Oscillation. *Monthly Weather Review*, *115*(10), 2262–2278. https://doi.org/10.1175/1520-0493(1987)115<2262:ameno>2.0.co;2

Zhang, R.-H., Kleeman, R., Zebiak, S. E., Keenlyside, N., & Raynaud, S. (2005). An empirical parameterization of subsurface entrainment temperature for improved SST anomaly simulations in an intermediate ocean model. *Journal of Climate*, *18*(2), 350–371. https://doi.org/10.1175/jcli-3271.1

Zhang, R.-H., Zebiak, S. E., Kleeman, R., & Keenlyside, N. (2003). A new intermediate coupled model for El Niño simulation and prediction. *Geophysical Research Letters*, *30*, 2012. https://doi.org/10.1029/2003gl018010

Zhang, W., Li, S., Jin, F. F., Xie, R., Liu, C., Stuecker, M. F., & Xue, A. (2019). ENSO regime changes responsible for decadal phase relationship variations between ENSO sea surface temperature and warm water volume. *Geophysical Research Letters*, *46*(13), 7546–7553. https://doi.org/10.1029/2019gl082943

Zheng, F., Zhu, J., Zhang, R.-H., & Zhou, G.-Q. (2006). Ensemble hindcasts of SST anomalies in the tropical Pacific using an intermediate coupled model. *Geophysical Research Letters*, *33*, L19604. https://doi.org/10.1029/2006gl026994

Zuo, H., Balmaseda, M. A., Tietsche, S., Mogensen, K., & Mayer, M. (2019). The ECMWF operational ensemble reanalysis-analysis system for ocean and sea ice: A description of the system and assessment. *Ocean Science*, *15*(3), 779–808. https://doi.org/10.5194/os-15-779-2019